

End-to-end Neuron Instance Segmentation based on Weakly Supervised Efficient UNet and Morphological Post-processing

Huaqian Wu¹, Nicolas Souedet¹, Caroline Jan¹, Cédric Clouchoux², Thierry Delzescaux¹

¹CEA-CNRS-UMR 9199, MIRCen, Fontenay-aux-Roses, France

²WITSEE, Neoxia, Paris, France

Keywords: *Neuron instance segmentation, weakly-supervised learning, mathematical morphology, microscopic images*

Abstract -- Recent studies have demonstrated the superiority of deep learning in medical image analysis, especially in cell instance segmentation, a fundamental step for many biological studies. However, the good performance of the neural networks requires training on large unbiased dataset and annotations, which is labor-intensive and expertise-demanding. In this paper, we present an end-to-end weakly-supervised framework to automatically detect and segment NeuN stained neuronal cells on histological images using only point annotations. We integrate the state-of-the-art network, EfficientNet, into our U-Net-like architecture. Validation results show the superiority of our model compared to other recent methods. In addition, we investigated multiple post-processing schemes and proposed an original strategy to convert the probability map into segmented instances using ultimate erosion and dynamic reconstruction. This approach is easy to configure and outperforms other classical post-processing techniques.

1. Introduction

Advances in microscopy techniques allow scanning whole slide images, capturing details at the cellular level and revealing the complexity of brain structures. It provides the opportunity to quantitatively analyze cell populations, their morphology and distribution to answer biological questions. For example, the number, distribution [1-3] and morphometric information [4] of neurons are important features to study brain aging including neurodegenerative diseases. A crucial prerequisite for carrying out such studies is cell instance segmentation, which plays a key role in digital pathology image analysis. Neuron segmentation is extremely challenging because the size, density, and intensity of neurons differ a lot from one anatomical region to another. Since manual identification of single cells is extremely laborious, several automatic segmentation algorithms have been proposed: thresholding [5], graph cut [6, 7] and watershed [8-10]. These methods need to be specifically adapted for different configurations (species, cell types, stainings). Furthermore, the segmentation results can be easily influenced by noise or other technical artifacts. Under-segmentation and over-segmentation often occur when they deal with touching or overlapping cells like neurons. You et al. [11] proposed a framework based on gaussian, min-max filter and region growing algorithm to deal with such data, but it is computationally expensive due to numerous iterations and it performed poorly on light-stained regions.

Recently, deep learning (DL) has achieved remarkable progress in many fields [12, 13], especially in medical image analysis, through convolutional neural networks (CNNs). DL-based methods have shown their superiority in cell segmentation competitions [14, 15], achieving better segmentations with stronger robustness compared to traditional algorithms. Naylor et al. [16] addressed this problem

as a regression task of estimating the nuclei distance map. A more common strategy is to address this problem as a semantic segmentation task, such as the pixel-wise binary classification of cells and background [17], or more recently the ternary classification of the interior of cells, background and cell boundaries [14, 18, 19]. Most CNNs such as AlexNet [20], VGGNet [21] and ResNet [22] learn representations by gradually reducing the size of feature maps, but the high-resolution features are lost during this process. These networks are not suitable for pixel-wise tasks like cell segmentation. Several networks add a resolution-recover process to address segmentation problems: SegNet [23] and DeconvNet [24] use unpooling and deconvolution layers to recover resolution; U-Net [25], a breakthrough in the field of medical image segmentation, with skip connections concatenate the high resolution features of the encoder path to the upsampled output of the decoder path. In our previous work [26], we evaluated an ensemble model of eight U-Net-like neural networks, with different backbone CNNs. More recently, Wang et al. proposed HRNet [27], which maintains high-resolution representations and assembles features from multi-resolution streams. It overperformed other state-of-the-art networks on several tasks of semantic segmentation, object detection as well as instance segmentation.

The good performance of CNNs relies on large datasets and the quality of pixel-level annotations, which are tedious and labor-intensive to be carried out manually. To facilitate the labeling process, several weakly-supervised methods investigated cell segmentation using point annotations: Qu et al. [28] trained a CNN to predict firstly the cell center location, and generated pixel-level labels using Voronoi transformation and k-means clustering. Based on a similar strategy, Chamanzar et al. [29] proposed a multi-task learning integrating repel encoding to enhance the segmentation performance. However, both [28] and [29] are not straightforward and involve multiple networks or branches respectively to achieve the final segmentations.

Moreover, CNNs without post-processing often failed to handle touching objects [16]. Researchers mainly focus on improving the performance of CNNs, while the post-processing part is generally not explicitly described although it is a critical step to obtain good segmentations. Applying watershed segmentation (WS) on the cell probability map derived from DL is the most common way [15, 30]. Graph partition [31] and distance transform [32] are also popular techniques. The winning method of [14] proposed a more tricky technique: a regression model was trained to predict the intersection-over-union (IoU) for cell candidates produced by applying different thresholds on the probability map. With this method, for one object, only the candidate with the highest IoU was preserved. One potential drawback of this method is that well-configured parameters are required to ensure the performance of these methods. Thus, this requires redesign the parameter settings for applications on novel data. Generic post-processing methods for cell instance segmentation are scarce and worth investigating.

In this paper, we propose an end-to-end weakly-supervised framework based on CNNs for neuron instance segmentation, with the following contributions: 1) we establish and validate a pixel-level-mask synthesis pipeline using only point annotations and Random Forest (RF) binary segmentations. It is able to generate a large labeled dataset with lower manual cost, 2) inspired by the instance segmentation challenge [33], we integrate EfficientNet-B5 [34] into a U-Net-like encoder-decoder architecture, this new model is spatially and semantically precise and 3) we propose a novel strategy for post-processing probability map based on ultimate erosion, dynamic reconstruction and WS. Our framework is generic and easy to configure: the only parameter to be adjusted is the size of the structuring element, which equals the size of the smallest cell in the dataset. We compare our network with other state-of-the-art CNNs methods [11, 25, 26, 27] for neuron

instance segmentation. The results demonstrate the superiority of our framework at both object-level and pixel-level making it possible to envision its use in biological studies.

2. Methods

2.1 Dataset

The data of this study are a set of two-dimensional (2D) light microscopy images. A representative histological section with a thickness of 40 μm was extracted from a healthy 9-year-old male macaque brain, stained by immunohistochemistry using the neuronal nuclei (NeuN) antibody, and scanned by an AxioScan.Z1 (Zeiss) with the resolution of 0.22 $\mu\text{m}/\text{pixel}$ ($\times 20$ magnification). The animal study was reviewed and approved by the Comité d'éthique agréé par le MESR dont relève l'EU: CETEA DSV – Comité n°44. Thirty images of 5000 \times 5000 pixels were selected to represent the heterogeneity of neuron distribution in the main anatomical regions, including cortex, hippocampus, thalamus, subiculum, etc (see Supplementary Fig. 1). These images showed a large diversity in terms of neuron size, shape, contrast and density, with both sparse (e.g. caudate and thalamus) and highly aggregated regions (e.g. cortex and hippocampus), as illustrated in Fig. 1. The pie chart presents the dataset composition in terms of anatomical regions, about 67% of images coming from the cortex and the hippocampus since the cortex is the largest brain structure (76%) [35] and hippocampal atrophy is linked to several neurodegenerative diseases [36]. All images were divided into two subsets: 24 images for the training set and 6 images for the test set. The test set contains the following regions: caudate, cortex ($\times 2$), hippocampus, subiculum and thalamus. Training images were cropped into 11k patches of 224 \times 224 pixels, $\frac{1}{4}$ of them were used to validate our neural networks at the end of each training epoch. To prevent overfitting and increase the robustness of the model, data augmentation was applied, including rotation, flipping, channel shuffling, color inversion, etc. The training set was expanded to 6 times compared to its original size.

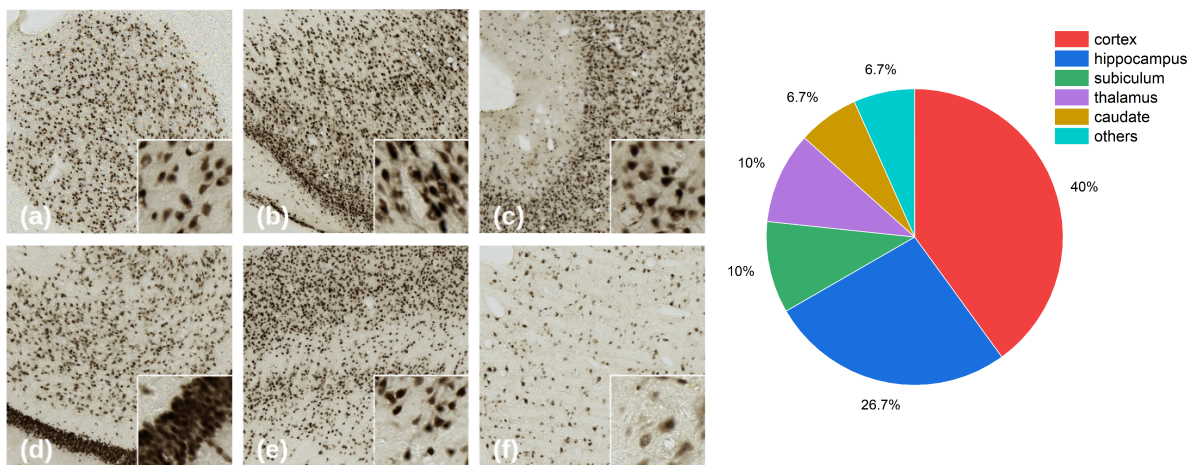


Fig.1 Example of the dataset. (a) caudate, (b,c) cortex, (d) hippocampus, (e) subiculum and (f) thalamus

To verify the representativeness of our test set, we extracted features of the dataset using a ResNet101 model [22] pre-trained on ImageNet and embedded the high-dimensional features into 2D space with t-distributed stochastic neighbor embedding (t-SNE) projection [37].

The images in the test set were evaluated at the large scale: they were firstly cropped into smaller patches (1344 \times 1344 pixels) with an overlap (120 pixels) in both vertical and horizontal directions. The size of patches is constrained by the GPU memory (16 GB). A weighted map [10] was applied on

the probability map of each patch to reduce the impact of inaccurate prediction at the border area, the weighted probability maps were then seamlessly assembled to reconstruct the probability map of the original large-scale image.

2.2 Pixel-level mask synthesis

In this study, we addressed neuron instance segmentation as a ternary classification task: neurons, background and contours of touching neurons. We designed a pipeline to synthesize pixel-level masks based on the point annotations (see Fig. 2): the neuron centroids were annotated manually in all the 30 images, by a disk with a radius of 5 pixels. In our previous work [11], a RF model with 100 decision trees was trained and optimized to perform binary segmentation of tissue and neurons using a subset of automatically selected features [38]. A competitive region growing algorithm was applied on the pin-pointed labels, using centroids as the seed to initialize the growing process, and the expansion was constrained by the binary segmentation of RF. On the labeled images, the pixels that connect different labels were identified as the third class of inter-cell contours and a thickness of 4 pixels was considered to separate touching or overlapping neurons. These 3-class-masks produced were used as the ground truth to train our neural network.

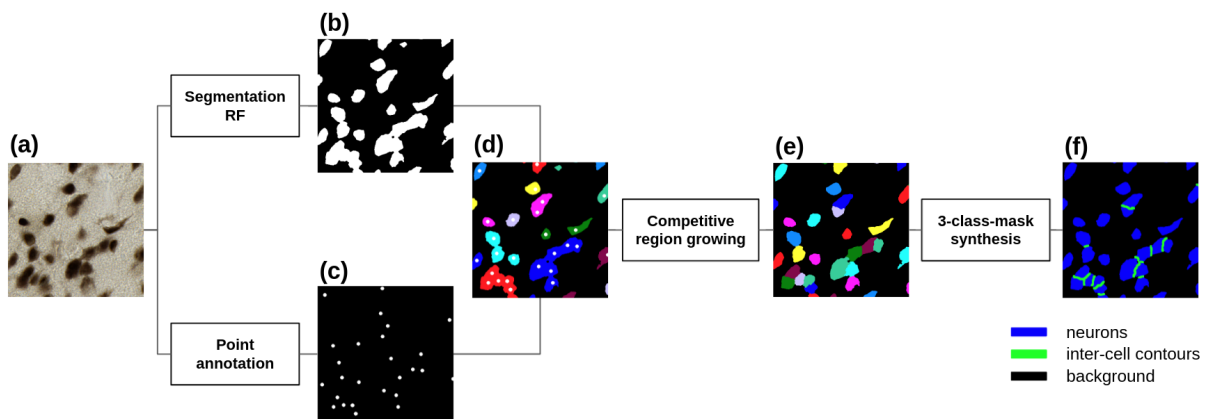


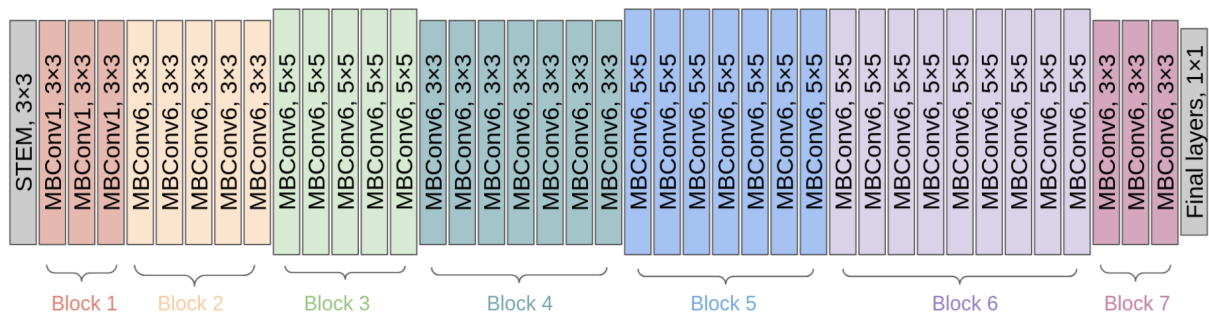
Fig. 2 Pixel-level mask synthesis. (a) original image, (b) RF binary segmentation, (c) manual point annotations, (d) fusion of colored connected components and (c), (e) labeled image produced by region growing and (f) final three-class-masks, blue: neurons, green: inter-cell contours and black: tissue.

To validate the synthetic mask generation process, three experts performed manual segmentation on a small dataset containing 5 patches of 500×500 pixels, including caudate, cortex ($\times 2$), hippocampus and subiculum. The average manual segmentation time of three experts was 2.5 hours.

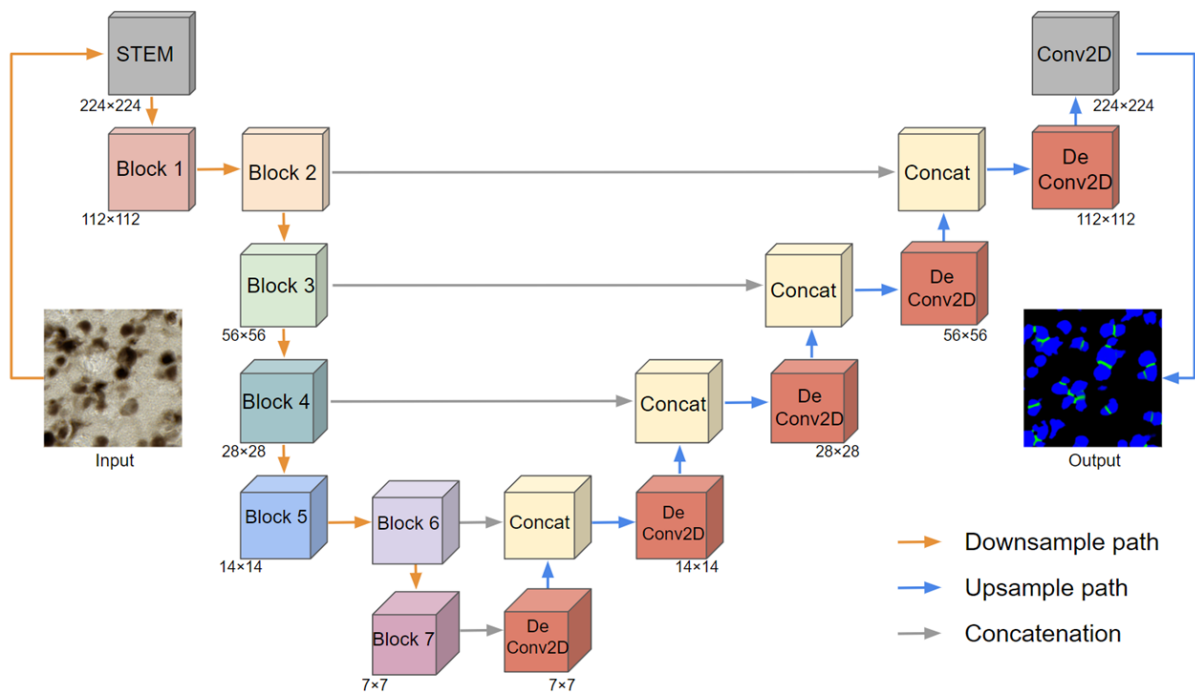
2.3 Neural networks

In our previous work [26], we showed the efficiency of U-Net-like architecture for neuron instance segmentation. Hence, we decided to keep the same strategy but with a more recent neural network as our backbone. The family of models called EfficientNets are proposed by Tan et al. [34], who showed superiority in accuracy and efficiency against previous CNNs. The baseline model, EfficientNet-B0,

was generated with multi-objective neural architecture search [34], its main building block is mobile inverted bottleneck MBConv [39]. Scaling up one network dimension of width, depth and input image resolution can improve accuracy, in particular, compound scaling of three dimensions can provide a significant gain [34]. This approach brought 7 scaled-up versions, named EfficientNet-B1 to EfficientNet-B7. EfficientNet-B5 was chosen as a result of a trade-off between accuracy and training cost. Fig. 4 (a) presents the architecture of EfficientNet-B5, consisting of stem layers, 7 main building blocks of MBConv and final layers. The resolution of the feature map was reduced five times gradually (from 224×224 to 7×7 pixels) after the stem layers, block 2, block 3, block 4 and block 6, respectively. Based on EfficientNet-B5 as the encoder, we gradually recovered the original high resolution through the decoder path, which consists of deconvolution and convolution layers. Fig. 4 (b) shows the structure of our network, named EfficientUNet-B5, skip connections concatenate encoder and decoder at 5 different resolutions.



(a)



(b)

Fig. 3 (a) The structure of EfficientNet-B5, it consists of 7 building MBConv blocks (represented with different color) and (b) the structure of our neural network using (a) as encoder, named EfficientUNet-B5, the encoder is concatenated with the decoder at five different resolution (Block 2, Block 3, Block 4, Block 6 and Block 7).

The compound loss of categorical cross-entropy (CE), soft dice loss [26][40] for neuron class and that for inter-cell contour class (D) was used to train the network. The global loss function L is defined as:

$$L = 0.5 CE + 0.3 D_{neuron} + 0.2 D_{contour} \quad (1)$$

$$CE = -\frac{1}{nc} \sum_{i,j} \sum_k^c t_{i,j,k} \log(p(i, j, k)) \quad (2)$$

$$D_k = 1 - \frac{2 \sum_{ij} t_{ij,k} p(i,j,k) + 1}{\sum_{ij} t_{ij,k} + \sum_{ij} p(i,j,k) + 1} \quad (3)$$

Where k denotes one class among c classes ($c = 3$), $t_{i,j,k}$ is equal to 1 if the pixel (i, j) belongs to class k , $p(i, j, k)$ denotes the probability of pixel (i, j) of being class k , n is the number of pixels in the patch. Cross-entropy was the most popular loss function for classification tasks. Soft dice loss [41] was adapted from the Dice coefficient, aimed to calculate the similarity between two images. One is added in numerator and denominator in (3) to ensure that the function is not undefined when $t_{i,j,k} = p(i, j, k) = 0$ [42]. Here, we associated CE with D for neurons and inter-cell contours to force the network to distinguish the two classes from the tissue. The numbers (0.5, 0.3 and 0.2), indicating the contribution of each item to the compound loss, are empirically defined constants and used to deal with class imbalance: CE and the sum of D (neuron and contour) have the same weight, while the weight of D_{neuron} is slightly higher than that of $D_{contour}$ because the neuron class is the most important class in our case.

The network was implemented in Tensorflow and Keras, weights of the encoder were pre-trained on ImageNet. The learning rate started from 1e-4 and decreased during the training. The model was trained for 100 epochs during 40h, with Adam optimizer.

2.4 Post-processing

Algorithm 1 presents our post-processing scheme. The output of our network P is an RGB image, presenting a 3-channel probability map, each channel corresponds to one class: channel R represents the background, channel G represents the contours between touching neurons and channel B represents neurons. Test Time Augmentations (TTA) of flipping ($\times 2$), rotation ($\times 4$) were applied, the prediction map was the average prediction of 8 patches. First, we extracted pixels that are most likely to be neuron class ($\text{argmax}(P) = neuron$), denoted these pixels to 1 and other pixels to 0 to create a binary image. Second, we applied the ultimate erosion on the binary image with a disk-shaped structuring element, the size equal to that of the smallest neuron [43], ensuring that no more than one neuron was erased during erosion to prevent under-segmentation. We believe that the inter-cell class could separate completely or partially the touching neurons. The second case often occurs in the dense region where the inter-cell class is not sufficient to entirely cut touching neurons, but it could create an initial concavity between cells, which would provide an optimal condition for performing ultimate erosion to complete the separation process. We labeled the ultimate residues, each residue representing an individualized neuron. Then, a dynamic reconstruction of dilation using the same structuring element was applied. Each residue was dilated with the same number of erosion that was estimated during ultimate erosion in order to primarily reconstruct each neuron shape close to their

actual size. The dilated residues may have an unnatural smooth shape due to the disk-shaped structuring element. To resolve this, we applied WS to further restore the morphologic information: the dilated residues were used as seeds to initialize the WS expansion, the expansion process was constrained by a binary mask constituted of neuron and inter-cell contour classes (1 if belongs to neuron or inter-cell contour, 0 otherwise). We merged the inter-cell contour channel and the neuron channel to restore the pixels lost due to our artificially created inter-cell class.

Algorithm 1 Post-processing using mathematical morphology

Input: three-channel probability map
Output: individualized neurons

- 1: Create binary mask based on neuron channel
- 2: Ultimate erosion with a disk S ($r = 10$ pixels)
- 3: **for** each ultimate residue U_i , **do**
- 4: $N_i \leftarrow$ number of erosion before U_i being removed
- 5: dilation with S , $U_i \leftarrow dil(U_i)$, $N_i \leftarrow N_i - 1$
- 6: repeat dilation until $N_i = 0$
- 7: **end for**
- 8: $M \leftarrow$ Combine neuron channel with inter-cell channel
- 9: apply WS, markers $\leftarrow U$, mask $\leftarrow M$
- 10: **return** segmented neurons

2.5 Evaluation

We aim to establish a framework to perform both neuron detection (object level) and neuron segmentation (pixel level). We matched predicted neurons with the point annotations to evaluate detection performance. A predicted neuron was considered as a true positive (TP) when it was superimposed with exactly one point annotation, otherwise, it was defined as a false positive (FP: not superimposed with any point label) or a false negative (FN: superimposed with more than one point label). FN also included the case that no neuron was detected in the location of a point label. With TP, FP and FN, we computed precision (P), recall (R) and F1 score (F-det) and relative count error (RCE) as follows:

$$P = \frac{TP}{TP + FP}; R = \frac{TP}{TP + FN}; F1 = \frac{2TP}{2TP + FP + FN} \quad (4)$$

$$RCE = \frac{|FP - FN|}{TP + FN} \quad (5)$$

RCE is the ratio of count error over the number of neurons identified with point labels.

Furthermore, we estimated how well-segmented neurons matched synthetic masks at pixel level. The IoU score $\frac{|A \cap B|}{|A \cup B|}$ was computed for all pairs of objects. Where A is a predicted neuron and B is the corresponding mask. When segmentation of a neuron covered the mask completely, the IoU score was 1. Since it is almost impossible to manually perform two identical segmentations, even for an expert, we selected 0.5 as the threshold of minimum IoU to identify correct segmentation, in this case: the TP was defined as the IoU greater than 0.5 between the predicted neuron and the synthetic mask, otherwise, it was a FP or a FN. With this new criterion, we computed the P, R and F1 score (F-seg) to

evaluate the segmentation performance. Dice coefficient and Aggregated Jaccard Index (AJI) [44] were also calculated to evaluate the segmentation at the pixel level. The AJI is defined as:

$$AJI = \frac{\sum_{i=1}^N |G_i \cap S(G_i)|}{\sum_{i=1}^N |G_i \cup S(G_i)| + \sum_{u=1}^U |S_u|} \quad (6)$$

Where G_i is one ground truth object, $S(G_i)$ is the segmented object that maximizes the IoU with G_i . U is the set of segmented objects that have not been assigned to any ground truth object.

This work was conducted on a workstation equipped with bi-processors (operating system: Ubuntu 16.04 LTS 64-bits, CPU: Intel Xeon gold 5218 at 2.3 GHz, RAM: 128 GB, GPU: NVIDIA Quadro RTX 5000 with 16 GB memory).

3. Results

In this section, we first show the representativeness of the test set versus the training set, see 3.1. Then, we present a quantitative evaluation of the synthetic mask generated using our pipeline in 3.2. In 3.3, we quantitatively compare our method with the state-of-the-art methods. In 3.4, we illustrate the advantage of our post-processing strategy in comparison with other classical techniques.

3.1 Qualitative evaluation of datasets composition

As shown in Fig 4, we plotted the heatmaps (number of bins = 25) based on the t-SNE projection of the whole dataset, the training set and the test set, respectively. X and Y were normalized to range [0,1], representing the two dimensions of the embedded space. Since test data have similar feature distribution (t-SNE plots of two distributions presents overlap) compared to that of training data, we can consider the test set as representative concerning the whole dataset.

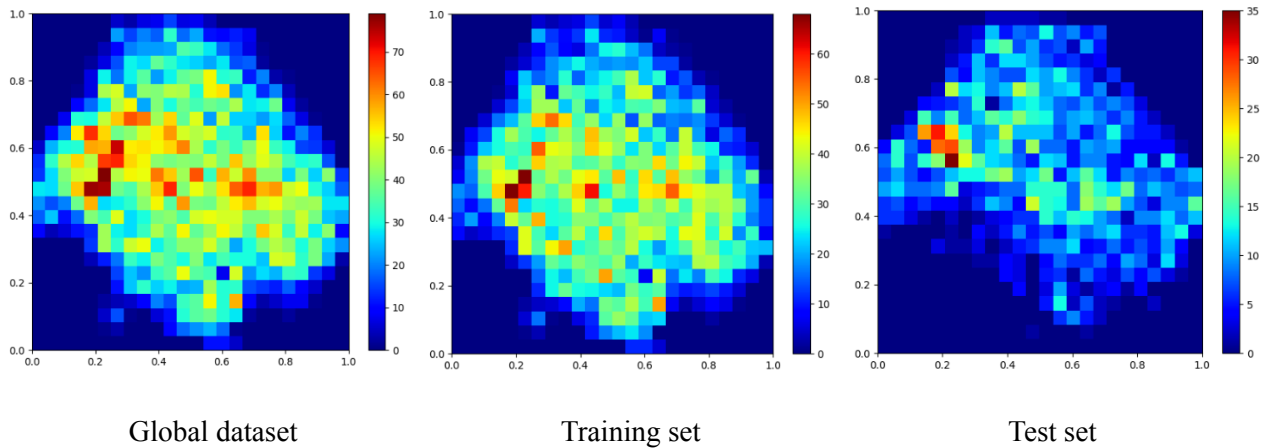


Fig. 4 Heatmaps of t-SNE projection. Left to right: all data, training data and test data.

3.2 Quantitative evaluation of synthetic mask

As mentioned above, our pipeline synthesized masks based on the manual point annotations, one neuron mask corresponded to one pin-point centroid. Therefore, we evaluate here only the expansion performance of our pipeline. Table 1 reports the average IoU score (mIoU) and Dice coefficient between the synthetic masks and three manual annotations (denoted as e1, e2 and e3) respectively, as well as the scores between manual annotations to show the inter-expert variability. We observe that the evaluation scores vary when we compare the synthetic masks to different manual annotations. Overall, our synthetic masks are of good quality, in particular, with e1 group as the reference. Fig. 5 shows some inconsistent manual segmentations. Globally, experts agree in most segmentations, with an average mIoU of 0.759 and Dice of 0.903, which is at the same level and slightly better than the results observed between our synthetic masks and manual segmentations (+2.4% for mIoU and +0.6% for Dice respectively).

Table 1 Quantitative analysis of synthetic mask in comparison with three experts

Evaluation metrics	Ours vs experts				inter-experts			
	ours vs e1	ours vs e2	ours vs e3	mean	e1 vs e2	e1 vs e3	e2 vs e3	mean
mIoU	0.774	0.706	0.724	0.735	0.753	0.769	0.755	0.759
Dice	0.914	0.888	0.888	0.897	0.898	0.91	0.9	0.903

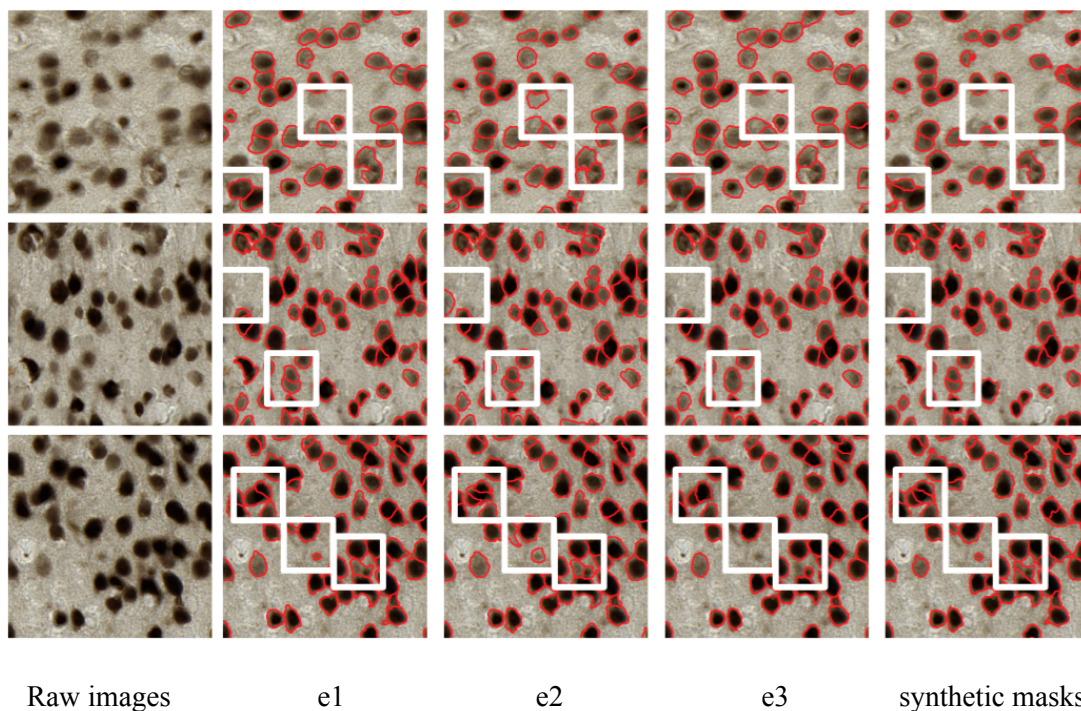


Fig. 5 Comparison of manual segmentations and synthetic masks. The white squares show the inconsistencies between manual segmentations.

3.3 Comparison with the state-of-the-art segmentation methods

Table 2 reports the performance of neuron detection (F1-det), neuron counting (RCE), semantic segmentation (Dice) and instance segmentation (F1-seg and AJI) of [11], UNet [18], Topcoders [14], HRNet [27], the proposed neural network. To eliminate the effect due to different post-processing schemes for CNNs based methods, we applied the same post-processing of Topcoders [14], which provided a better segmentation compared to classical post-processing. Overall, our method is the most competing one on Dice, F1-seg and AJI. At the object level, especially F1-det and RCE, HRNet has almost identical performance as the proposed approach. They are slightly lower than that of Topcoders, while they outperform others on F1-seg. We observe a more significant improvement brought by our method at the pixel level (Dice and AJI). Topcoders is the best method of neuron detection and counting, but it is less competitive in preserving the morphological information of neurons (Dice and AJI). HRNet achieves the same score as our method on detection, and it outperforms almost most methods at the pixel level except our method. We did not compute the Dice for the unsupervised method [11], because it used the same binary RF segmentation that constrained our synthetic masks. [11] made several errors on neuron detection and counting, yet it achieves good results on segmentation tasks: it is at the same level as Topcoders on F1-seg and HRNet on AJI. However, UNet achieves the worst results on all the tasks, at both object and pixel level.

Table 2 Neuron detection, counting and instance segmentation of different automatic methods. The best results are in bold.

	[11]	UNet	Topcoders	HRNet	Proposed
F1-det	0.889	0.819	0.931	0.924	0.924
RCE(%)	7.56	26.36	2.58	4.4	4.37
Dice	-	0.89	0.918	0.933	0.934
F1-seg	0.87	0.715	0.88	0.895	0.901
AJI	0.729	0.473	0.709	0.732	0.742

Fig. 6 provides an overall comparison of both object level (F1-seg) and pixel level (AJI). In terms of F1-seg, the proposed network outperforms others and it is also the most robust, with less than 4% differences between anatomical regions. HRNet also has good performance but the scores are slightly lower than ours. Although Topcoders works well in certain regions (maximum value higher than others), its median and mean F1-seg are lower than HRNet and the proposed network. The unsupervised method [11] performs less well globally but it is stable for the majority of regions, most scores are around 0.87, with two outliers above and below the interquartile range. AJI illustrates differences between methods in a more significant way. Our method is the best, followed by HRNet. With this criteria, the scores of Topcoders drop and the interquartile range is lower than the other two methods. By contrast, [11] is the second-last method of detection, while it performs better than Topcoders on segmentation, with AJI scores at the same level as HRNet. Both F1-seg and AJI confirm the poor performance of UNet on neuron detection and instance segmentation.

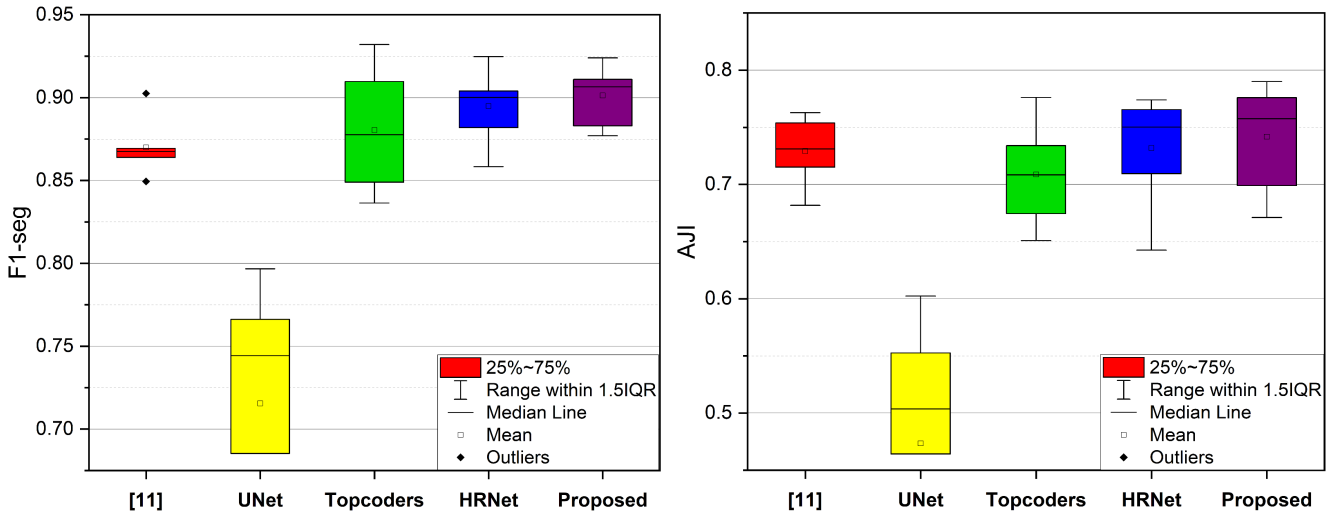
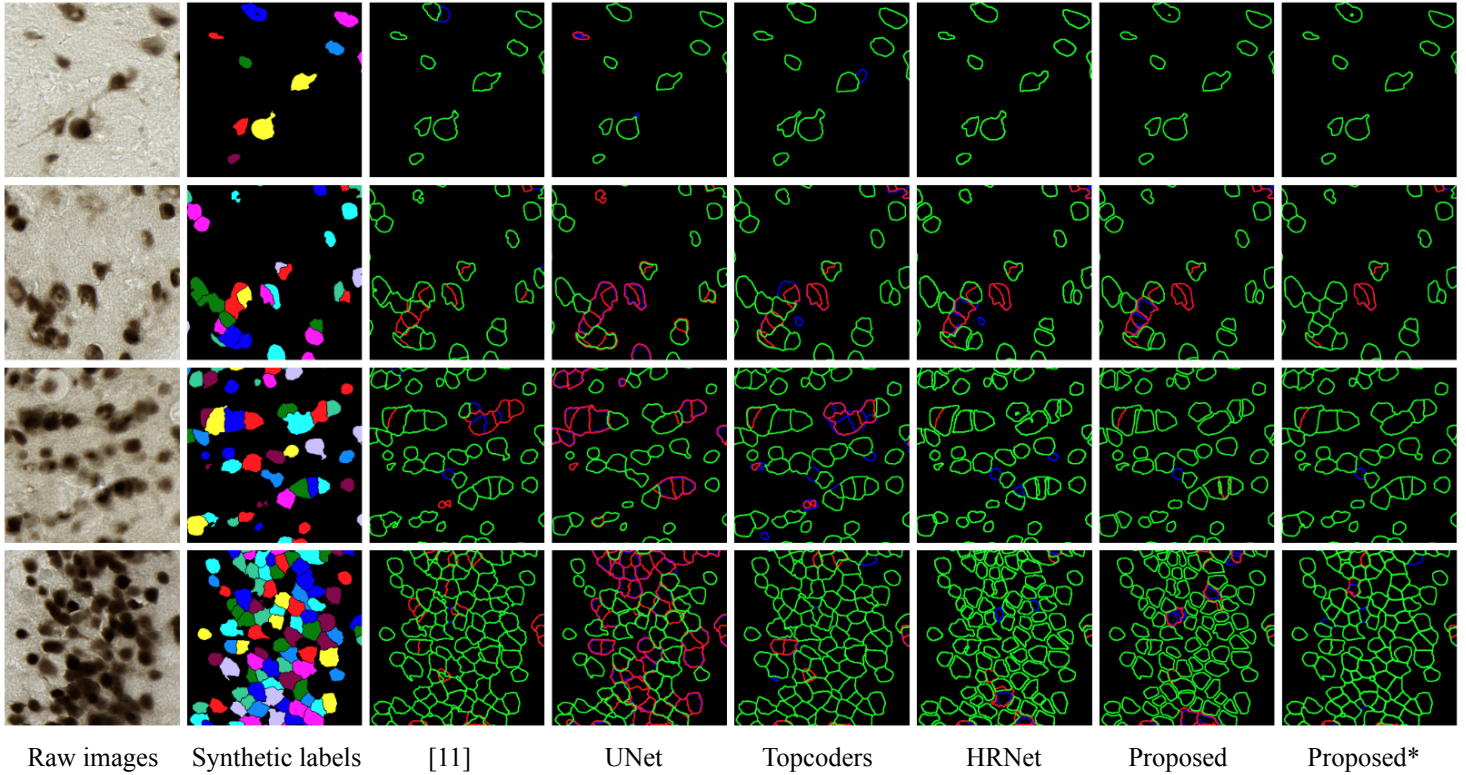


Fig. 6 Boxplot of F1-seg and AJI for different methods for comparative analysis. Left panel: F1 scores of segmentation. Right panel: AJI scores(outlier values of UNet are below the vertical scale range).

Fig. 7 shows comparison and representative patches from different anatomical regions. Besides the methods mentioned above (in Table 2 and Fig. 6), we also report the segmentation results of the complete proposed pipeline (network and post-processing) to visualize the improvement brought by the proposed post-processing. If the IoU between a segmented object and the ground truth is superior to 0.5, we highlight the contours in green. Otherwise, the contours are displayed either in blue for over-segmentation or in red for under-segmentation and missing detection respectively. [11] segments most neurons correctly in sparse regions, while under-segmentation often occurs when the neurons aggregate. UNet suffers from under- and missing segmentation, but it is also not effective in preserving the shape of neurons. Globally, Topcoders performs better than [11] and UNet, although it sometimes over-segments the neurons. HRNet achieves promising results in most regions, even in the hippocampus. Our method outperforms the others in all anatomical regions, from the thalamus (sparse) to the hippocampus (dense), with better shape preservation.



* Segmentation results using the proposed post-processing

Fig. 7 Original images and segmentation results of our method and other approaches in different regions with different neuron density. Top to Down: (1) thalamus, (2) caudate, (3) cortex and (4) hippocampus. The green contours represent segmentations that overlap (IoU > 0.5) the synthetic ground truth, the blue contours represent over-segmentations and the red contours represent missing / under-segmentations.

3.4 Validation of our post-processing strategy in comparison with classical post-processing

We compare the segmentation performance of the proposed post-processing to the classical methods using the same probability maps (EfficientUNet-B5) in Table 3. The most popular post-processing is to apply WS on the thresholded cell channel ($th \geq 0.5$) of the probability map, which is used as a baseline in this study. We also apply the state-of-the-art techniques, the winning method of [14], for comparison. According to the results of the baseline (both F1-seg and AJI), the neural network performs well in high contrast region (subiculum) and in the region where only a few neurons overlap (caudate), the performance decreases as the density of neurons increases (hippocampus), and in the region where neurons have low contrast with the background (thalamus). In terms of F1-seg, the regression model of [14] brings a slight improvement (2.2%) compared to the baseline, especially in sparse regions with light-stained neurons: F1-seg is increased by 3.5% in the thalamus. Our post-processing further improves the segmentation with a 4% gain over the baseline. In particular for dense regions like the cortex (4.5%) and the hippocampus (4.5%). In terms of AJI, the improvement brought by [14] is less significant (1.7% on average). The region with the greatest increase of AJI is the cortex, by 3.1%. On the contrary, with AJI, we observe a more significant improvement of 4.6% with our method. The gain is even greater in the cortex (7.7%) and hippocampus (6.3%) regions.

Table 3 Segmentation performance using different post-processing techniques. The best results are in bold.

Anatomical region	F1-seg			AJI		
	baseline	[14]	Proposed	baseline	[14]	Proposed
caudate	0.885	0.903	0.916	0.754	0.775	0.79
cortex	0.87	0.896	0.915	0.689	0.72	0.766
hippocampus	0.857	0.877	0.902	0.661	0.671	0.724
subiculum	0.912	0.924	0.940	0.783	0.79	0.821
thalamus	0.876	0.911	0.916	0.76	0.776	0.777
overall	0.878	0.901	0.917	0.723	0.742	0.774

Fig. 8 presents the results for each intermediate step of our post-processing scheme. The inter-cell class allows our neural network to segment the sparse region like caudate and most neurons in the cortex without any problem. However, our network sometimes fails to separate touching neurons as illustrated by the red square in Fig. 8 (b, c). This problem becomes troublesome for the hippocampus region, where many neurons aggregate, which would cause the under-estimation of neuron population. In this particular case, the ultimate erosion process in our scheme brings a critical advantage: although the inter-cell class did not completely separate the touching neurons, it provided an optimal condition to apply further erosion: an initial concavity. Fig. 8 (d) shows the ultimate residues, we observe that the neurons that have not been separated by the neural network are now fully segmented. By applying the same iteration number of dilation with the same structuring element as erosion on each ultimate residue, we restore seeds with the coarse morphological information of neurons, as illustrated in Fig. 8 (e). Furthermore, the WS process using dilated residues as seeds is particularly robust. The combination of inter-cell and neuron classes as expansion constraints, allows recovery of the neuron shape more precisely by reassigning inter-cell pixels to neurons.

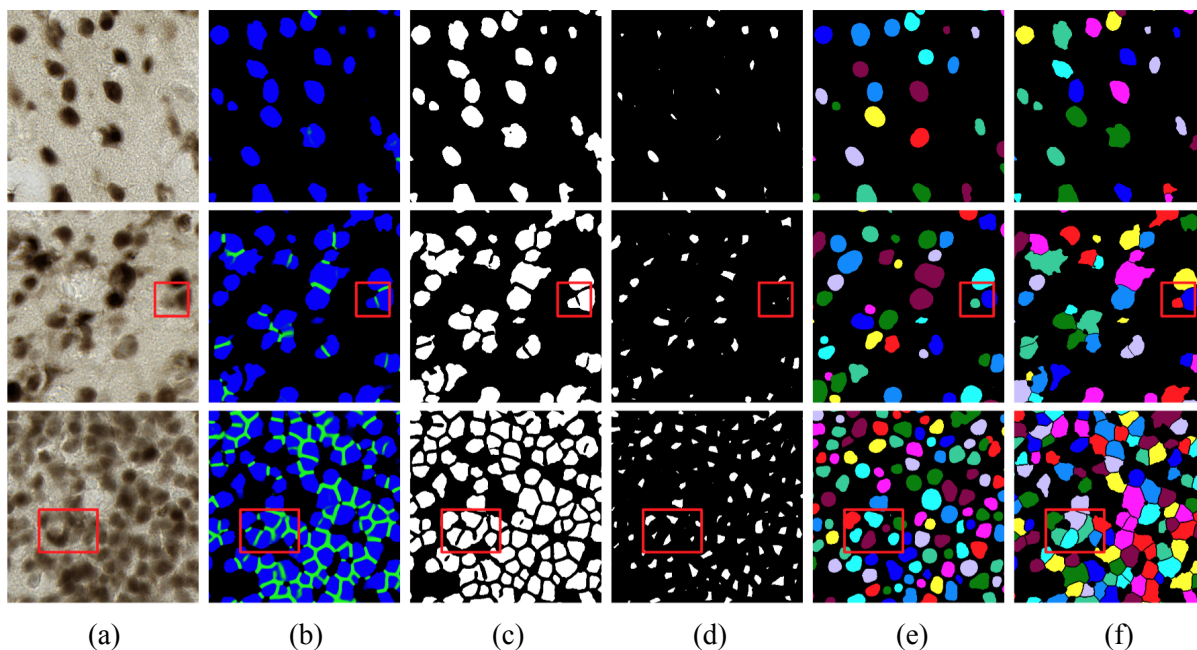


Fig. 8 Intermediate results of proposed post-processing. Top to down: (1) caudate, (2) cortex and (3) hippocampus. Left to right: (a) original images, (b) probability map of deep network, (c) binary mask of neuron channel, (d) ultimate residues, (e) reconstructed residues and (f) final segmentation. The red square highlights the neurons that the neural network failed to separate but being fully segmented through the proposed post-processing.

4. Discussion

Unbiased quantification of cells is required for many biomedical analyses. One challenging application field is to count and study the neuronal cells as their shape, population and density vary from one anatomical region to another. Recent studies proved the importance of neuron morphology and distribution to study cerebral functions and neurodegenerative diseases [1-4]. An automatic neuron segmentation method is therefore a cornerstone for such research. In this work, we present an end-to-end weakly-supervised framework aiming to improve neuron detection and instance segmentation in the major anatomical regions of the macaque brain. Based on pin-pointed centroids and RF binary segmentation, our mask synthesis pipeline allowed us to generate large amounts of pixel-level annotations for training. In addition, embedding the state-of-the-art CNN (EfficientNet-B5) to a UNet-like architecture increased segmentation accuracy. Although mathematical morphology techniques such as ultimate erosion for segmenting connected components [45] have been proposed decades ago, it requires a strong prerequisite of concavity between the connected components to obtain good results especially in dense regions presenting highly aggregated cells. Here, this condition was satisfied by adding the inter-cell class in the probability map. Furthermore, we proposed a novel technique, dynamic reconstruction, to achieve more robust morphological reconstruction.

Table 1 and Fig. 5 reveal the good quality of the synthetic annotation with similar variability between our pipeline and experts as within experts, with a drop of 2.4% in mIoU and 0.6% in Dice. Table 2 and Fig. 6 provide a comparative analysis of the proposed network versus other approaches. The proposed network outperforms others on segmentation tasks (Dice, F1-seg and AJI), it achieves

similar performance on neuron detection compared to Topcoders. However, our network performs less well (-0.2%) than Topcoders on neuron counting, since the counting error only takes into account the total number of neurons segmented in the image, under- and over-segmentation occasionally compensate for each other. Indeed, Topcoders suffers from both under- and over-segmentation, whereas under-segmentation exists as the main problem for other approaches, including ours, as illustrated in Fig. 7. According to the quantitative evaluation (Table 2 and Fig. 6), the performance of HRNet is comparable to that of the proposed network. But both of them create an artificial inter-cell contour for the touching neurons, especially in the dense regions such as the hippocampus, as shown in Fig. 7. One explanation is that the applied post-processing scheme used the thresholded neuron class probability map as the WS mask to constraint the final expansion. In the probability maps of HRNet and the proposed method, all three classes are generally well classified. In contrast, in the probability maps of the other methods (UNet and Topcoders), the predictions of the inter-cell class are less precise and often mixed with those of the neuron class. This results in a larger WS mask where the neuron class merges pixels of the inter-cell contour class. Our post-processing results (last column of Fig. 7) demonstrate that this contradiction could be eliminated by merging the neuron and the inter-cell classes as WS mask. The performance of the unsupervised method [11] is stable for most anatomical regions, with two outliers in Fig. 6. It is probably because the fixed parameter settings are not suitable for some of the tested regions. Topcoders and our method confirm the efficiency of UNet-like architecture on segmentation tasks. However, the basic UNet performs poorly in almost all tested regions, owing to the fact that the depth and width of UNet are not sufficient to capture such complex features of neurons.

Table 3 compares the segmentation performance of three post-processing techniques on different anatomical regions. Even with a simple combination of threshold and WS, the baseline achieves promising results with the probability map produced with EfficientUNet-B5. The regression model of [14] provides improvements by reducing FP objects, while our method further increases the accuracy on both F1-seg and AJI using mathematical morphology. In particular, our method yields significant gains in high-density regions, through separating the touching neurons that have not been well segmented with the probability maps, especially in the region of cortex and hippocampus, as illustrated by the red squares in Fig. 8. On the other hand, in sparse regions, such as the caudate and the thalamus, the superiority of our method becomes less significant, since the neural network is able to correctly segment the neurons in these regions. Still, we observe better segmentation results with our method in these regions. It is possibly linked to the fact that the use of dynamically reconstructed residues to initialize the expansion led to a more accurate preservation of the neuron shape. In addition to a better segmentation accuracy, our post-processing has also the benefit of being generic: it can be easily applied to other nuclei data or species, the only parameter to be adjusted being the size of the structuring element used for morphological operations, which corresponds to the size of the smallest cell.

Taken together, our framework is competitive on both detection and instance segmentation tasks compared to other reference approaches. From point annotations to pixel-level neuron individualization, it performs well on all tested anatomical regions, with easier parameter settings.

5. Conclusion

In this paper, we present a weakly-supervised end-to-end DL framework to perform neuron detection and instance segmentation. A major problem with neural networks is the lack of precise annotations. We proposed a mask-synthesis pipeline to generate pixel-level labels using only point annotations, which considerably reduced the manual labeling effort, and we confirmed the quality of synthetic masks by comparing them with three manual segmentation sets. By implementing EfficientNet-B5 as encoder, we demonstrated the efficiency of UNet-like architecture on segmentation, and our network outperformed previously published methods in multiple object and pixel level evaluations. Through ultimate erosion and dynamic reconstruction, our post-processing scheme improved the segmentation of the neural network. In particular, the excellent performance in the regions of cortex and hippocampus enables us to envision the assessment of more information related to brain functions and neurodegenerative diseases. In the future, we would work on the optimization of codes, developments in high-performance computing involving CPU and GPU, to extend this study to the whole histological section and even the entire brain, which would help us to better understand brain development and aging. From a broader perspective, our method can be adapted to other species. As a preliminary study, it was successfully applied to the cerebral cortex of mouse (Supplementary Fig. 2) and mouse lemur (*Microcebus murinus*) primate (Supplementary Fig. 3 [46]).

Declaration of Competing Interests

The authors declare that they have no known competing financial interests or personal relationships that could have appeared to influence the work reported in this paper.

Acknowledgement

The authors wish to thank the anonymous reviewers for their insightful comments and suggestions. This work was supported by DIM ELICIT grants from Région Ile-de-France. The authors would like to acknowledge Camille Mabillon for manual segmentation, Zhenzhen You for point annotation and Géraldine Liot, Suzanne Lam, Fanny Petit and Marc Dhenain for providing supplementary mouse and *Microcebus* brain images.

Reference

1. Thu D C V, Oorschot D E, Tippett L J, et al. Cell loss in the motor and cingulate cortex correlates with symptomatology in Huntington's disease. *Brain*, 2010, 133(4): 1094-1110. <https://doi.org/10.1093/brain/awq047>
2. Karlsen A S, Pakkenberg B. Total numbers of neurons and glial cells in cortex and basal ganglia of aged brains with Down syndrome—a stereological study. *Cerebral cortex*, 2011, 21(11): 2519-2524. <https://doi.org/10.1093/cercor/bhr033>
3. Hughes C C W, Lantos P L. A morphometric study of blood vessel, neuron and glial cell distribution in young and old rat brain. *Journal of the neurological sciences*, 1987, 79(1-2): 101-110. [https://doi.org/10.1016/0022-510x\(87\)90264-4](https://doi.org/10.1016/0022-510x(87)90264-4)
4. Vicar T, Raudenska M, Gumulec J, et al. The quantitative-phase dynamics of apoptosis and lytic cell death. *Scientific reports*, 2020, 10(1): 1-12. <https://doi.org/10.1038/s41598-020-58474-w>

5. Otsu N. A threshold selection method from gray-level histograms. *IEEE transactions on systems, man, and cybernetics*, 1979, 9(1): 62-66. <https://doi.org/10.1109/tsmc.1979.4310076>
6. Lou X, Koethe U, Wittbrodt J, et al. Learning to segment dense cell nuclei with shape prior. 2012 IEEE Conference on Computer Vision and Pattern Recognition. IEEE, 2012: 1012-1018. <https://doi.org/10.1109/cvpr.2012.6247778>
7. He Y, Gong H, Xiong B, et al. iCut: an integrative cut algorithm enables accurate segmentation of touching cells. *Scientific reports*, 2015, 5(1): 1-17. <https://doi.org/10.1038/srep12089>
8. Cousty J, Bertrand G, Najman L, et al. Watershed cuts: Minimum spanning forests and the drop of water principle. *IEEE transactions on pattern analysis and machine intelligence*, 2008, 31(8): 1362-1374. <https://doi.org/10.1109/tpami.2008.173>
9. Veta M, Huisman A, Viergever M A, et al. Marker-controlled watershed segmentation of nuclei in H&E stained breast cancer biopsy images. 2011 IEEE international symposium on biomedical imaging: from nano to macro. IEEE, 2011: 618-621. <https://doi.org/10.1109/isbi.2011.5872483>
10. Veta M, Van Diest P J, Kornegoor R, et al. Automatic nuclei segmentation in H&E stained breast cancer histopathology images. *PloS one*, 2013, 8(7): e70221. <https://doi.org/10.1371/journal.pone.0070221>
11. You Z, Balbastre Y, Bouvier C, et al. Automated individualization of size-varying and touching neurons in macaque cerebral microscopic images. *Frontiers in neuroanatomy*, 2019, 13: 98. <https://doi.org/10.3389/fnana.2019.00098>
12. LeCun Y, Bengio Y, Hinton G. Deep learning. *nature*, 2015, 521(7553): 436-444. <https://doi.org/10.1038/nature14539>
13. Liu W, Wang Z, Liu X, et al. A survey of deep neural network architectures and their applications. *Neurocomputing*, 2017, 234: 11-26. <https://doi.org/10.1016/j.neucom.2016.12.038>
14. Caicedo J C, Goodman A, Karhohs K W, et al. Nucleus segmentation across imaging experiments: the 2018 Data Science Bowl. *Nature methods*, 2019, 16(12): 1247-1253. <https://doi.org/10.1038/s41592-019-0612-7>
15. Kumar N, Verma R, Anand D, et al. A multi-organ nucleus segmentation challenge. *IEEE transactions on medical imaging*, 2019, 39(5): 1380-1391. <https://doi.org/10.1109/TMI.2019.2947628>
16. Naylor P, Laé M, Reyat F, et al. Segmentation of nuclei in histopathology images by deep regression of the distance map. *IEEE transactions on medical imaging*, 2018, 38(2): 448-459. <https://doi.org/10.1109/TMI.2018.2865709>
17. Sirinukunwattana K, Raza S E A, Tsang Y W, et al. Locality sensitive deep learning for detection and classification of nuclei in routine colon cancer histology images. *IEEE transactions on medical imaging*, 2016, 35(5): 1196-1206. <https://doi.org/10.1109/tmi.2016.2525803>
18. Cui Y, Zhang G, Liu Z, et al. A deep learning algorithm for one-step contour aware nuclei segmentation of histopathology images. *Medical & biological engineering & computing*, 2019, 57(9): 2027-2043. <https://doi.org/10.1007/s11517-019-02008-8>
19. Chen H, Qi X, Yu L, et al. DCAN: Deep contour-aware networks for object instance segmentation from histology images. *Medical image analysis*, 2017, 36: 135-146. <https://doi.org/10.1016/j.media.2016.11.004>
20. Krizhevsky A, Sutskever I, Hinton G E. ImageNet classification with deep convolutional neural networks. *Communications of the ACM*, 2017, 60(6): 84-90. <https://doi.org/10.1145/3065386>

21. Simonyan K, Zisserman A. Very deep convolutional networks for large-scale image recognition. 2015 International Conference on Learning Representations. <https://arxiv.org/abs/1409.1556>
22. He K, Zhang X, Ren S, et al. Deep residual learning for image recognition. Proceedings of the IEEE conference on computer vision and pattern recognition. 2016: 770-778. <https://doi.org/10.1109/cvpr.2016.90>
23. Badrinarayanan V, Kendall A, Cipolla R. Segnet: A deep convolutional encoder-decoder architecture for image segmentation. IEEE transactions on pattern analysis and machine intelligence, 2017, 39(12): 2481-2495. <https://doi.org/10.1109/tpami.2016.2644615>
24. Noh H, Hong S, Han B. Learning deconvolution network for semantic segmentation. Proceedings of the IEEE international conference on computer vision. 2015: 1520-1528. <https://doi.org/10.1109/ICCV.2015.178>
25. Ronneberger O, Fischer P, Brox T. U-net: Convolutional networks for biomedical image segmentation. International Conference on Medical image computing and computer-assisted intervention. Springer, Cham, 2015: 234-241. https://doi.org/10.1007/978-3-319-24574-4_28
26. Wu H, Souedet N, You Z, et al. Evaluation of Deep Learning Topcoders Method for Neuron Individualization in Histological Macaque Brain Section. 2021 43rd Annual International Conference of the IEEE Engineering in Medicine & Biology Society (EMBC). IEEE, 2021: 2985-2988. <http://dx.doi.org/10.1109/EMBC46164.2021.9630914>
27. Wang J, Sun K, Cheng T, et al. Deep high-resolution representation learning for visual recognition. IEEE transactions on pattern analysis and machine intelligence, 2020. <https://doi.org/10.1109/tpami.2020.2983686>
28. Qu H, Wu P, Huang Q, et al. Weakly supervised deep nuclei segmentation using partial points annotation in histopathology images. IEEE Transactions on Medical Imaging, 2020, 39(11): 3655-3666. <https://doi.org/10.1109/tmi.2020.3002244>
29. Chamanzar A, Nie Y. Weakly supervised multi-task learning for cell detection and segmentation. 2020 IEEE 17th International Symposium on Biomedical Imaging (ISBI). IEEE, 2020: 513-516. <https://doi.org/10.1109/isbi45749.2020.9098518>
30. Xie L, Qi J, Pan L, et al. Integrating deep convolutional neural networks with marker-controlled watershed for overlapping nuclei segmentation in histopathology images. Neurocomputing, 2020, 376: 166-179. <https://doi.org/10.1016/j.neucom.2019.09.083>
31. Song Y, Zhang L, Chen S, et al. Accurate segmentation of cervical cytoplasm and nuclei based on multiscale convolutional network and graph partitioning. IEEE Transactions on Biomedical Engineering, 2015, 62(10): 2421-2433. <https://doi.org/10.1109/tbme.2015.2430895>
32. Xing F, Xie Y, Yang L. An automatic learning-based framework for robust nucleus segmentation. IEEE transactions on medical imaging, 2015, 35(2): 550-566. <https://doi.org/10.1109/TMI.2015.2481436>
33. Van Etten A, Hogan D. The SpaceNet Multi-Temporal Urban Development Challenge. arXiv preprint arXiv:2102.11958, 2021. <https://arxiv.org/abs/2102.11958>
34. Tan M, Le Q. Efficientnet: Rethinking model scaling for convolutional neural networks. International Conference on Machine Learning. PMLR, 2019: 6105-6114. <http://proceedings.mlr.press/v97/tan19a/tan19a.pdf>
35. Frahm H D, Stephan H, Stephan M. Comparison of brain structure volumes in Insectivora and Primates. I. Neocortex. Journal fur Hirnforschung, 1982, 23(4): 375-389.
36. Anand K S, Dhikav V. Hippocampus in health and disease: An overview. Annals of Indian Academy of Neurology, 2012, 15(4): 239. <https://dx.doi.org/10.4103%2F0972-2327.104323>

37. Van der Maaten L, Hinton G. Visualizing data using t-SNE. *Journal of machine learning research*, 2008, 9(11).
<https://www.jmlr.org/papers/volume9/vandermaaten08a/vandermaaten08a.pdf?fbclid=IwA>
38. Bouvier C, Souedet N, et al. Reduced and stable feature sets selection with random forest for neurons segmentation in histological images of macaque brain. *Scientific reports*, 2021, 11(1), 1-17.
39. Sandler M, Howard A, Zhu M, et al. Mobilenetv2: Inverted residuals and linear bottlenecks. *Proceedings of the IEEE conference on computer vision and pattern recognition*. 2018: 4510-4520. <https://doi.org/10.1109/CVPR.2018.00474>
40. Zhou Z, Siddiquee M M R, Tajbakhsh N, et al. Unet++: Redesigning skip connections to exploit multiscale features in image segmentation. *IEEE transactions on medical imaging*, 2019, 39(6): 1856-1867.
41. Milletari F, Navab N, Ahmadi S A. V-net: Fully convolutional neural networks for volumetric medical image segmentation. *2016 fourth international conference on 3D vision (3DV)*. IEEE, 2016: 565-571.
42. Jadon S. A survey of loss functions for semantic segmentation. *2020 IEEE Conference on Computational Intelligence in Bioinformatics and Computational Biology (CIBCB)*. IEEE, 2020: 1-7. <https://doi.org/10.1109/CIBCB48159.2020.9277638>
43. Andersen P, Morris R, Amaral D, et al. *The hippocampus book*. Oxford university press, 2006.
44. Kumar N, Verma R, Sharma S, et al. A dataset and a technique for generalized nuclear segmentation for computational pathology. *IEEE transactions on medical imaging*, 2017, 36(7): 1550-1560. <https://doi.org/10.1109/TMI.2017.2677499>
45. Vincent L, Beucher S. *The morphological approach to segmentation: an introduction*. Centre de Morphologie Mathématique, Ecole Nationale Supérieure des Mines de Paris, 1989.
<https://people.cmm.minesparis.psl.eu/users/beucher/publi/IntroSegmentTools.pdf>
46. Gary C, Lam S, et al. Encephalopathy induced by Alzheimer brain inoculation in a non-human primate. *Acta neuropathologica communications*, 2019, 7(1), 1-21.